Long-lived electronic coherences in molecular wave packets probed with pulse-shape spectroscopy

Brian Kaufman,[1] Philipp Marquetand,[2] Tamás Rozgonyi,[3] and Thomas Weinacht[1]
[1]*Department of Physics and Astronomy, Stony Brook University, Stony Brook, New York 11794-3800, USA*
[2]*Institute of Theoretical Chemistry, Faculty of Chemistry, University of Vienna, Währinger Strasse 17, 1090 Vienna, Austria*
[3]*HUN-REN Wigner Research Centre for Physics, P.O. Box 49, 1525 Budapest, Hungary*

(Received 15 February 2024; accepted 5 August 2024; published 25 September 2024)

We explore long-lived electronic coherences in molecules using shaped ultrafast laser pulses to launch and probe entangled nuclear-electronic wave packets. We find that for particular pairs of states, the electronic phase remains well defined despite vibrational motion along many degrees of freedom. We explore the time dependence of the electronic coherence and show how it is modulated by the time-dependent vibrational overlap between the two wave functions. Our measurements are interpreted with electronic structure calculations and compared to analytic expressions for the electronic coherence.

DOI: 10.1103/PhysRevA.110.033118

I. INTRODUCTION

The motion of electrons in photoexcited molecules drives many basic light-driven processes in physics, chemistry, and biology. From solar cells to photodissociation and photosynthesis, electronic dynamics play a fundamental role in molecular transformation and can determine what the final products are [1]. Electronic dynamics can be described in terms of wave packets—coherent superpositions of electronic eigenstates, whose evolution is dictated by the relative phase between states [2–4]. While this phase relationship ("electronic coherence") remains well defined in atoms for many cycles [5–8], in molecules it is complicated by the motion of the nuclei, which are entangled with the electrons; i.e., the full wave function generally cannot be written as a product of electronic and nuclear wave functions, and the entanglement of the wave function typically leads to a rapid decay in the electronic coherence if one does not perform nuclear-coordinate-resolved measurements.

The loss of electronic coherence as a consequence of electron-nuclear coupling can be seen by considering the total wave function as a Born-Oppenheimer or Born-Huang expansion [9]:

$$\Psi(\boldsymbol{r},\boldsymbol{R},t)=\sum_n a_n\chi_n(\boldsymbol{R},t)\psi_n(\boldsymbol{r};\boldsymbol{R})e^{-i\omega_n t}, \tag{1}$$

where $\boldsymbol{r}$ and $\boldsymbol{R}$ represent the electronic and nuclear degrees of freedom, respectively, $\psi_n(\boldsymbol{r};\boldsymbol{R})$ represents the nth electronic eigenstate of the molecule, a_n is the complex amplitude of the nth state (which, in principle, can be time dependent due to nonadiabatic coupling between the electronic states), ω_n represents the nth electronic eigenstate frequency, and $\chi_n(\boldsymbol{R},t)$ represents the (normalized) time-dependent nuclear wave function in the nth electronic state [10]. As shown in earlier work [11], the excitation of such a wave packet leads to an electronic coherence which is given by the off-diagonal element of the density matrix and can be written as

$$\rho_{12}(\boldsymbol{R},t)=a_1\chi_1(\boldsymbol{R},t)a_2^*\chi_2^*(\boldsymbol{R},t)e^{i(\omega_2-\omega_1)t}, \tag{2}$$

where $\hbar\omega_1=V_1$ and $\hbar\omega_2=V_2$, where V_1 and V_2 represent the minimum potential energies of states 1 and 2, respectively. Calculations and measurements over the past two decades have established rather short lifetimes for $\rho_{12}(\boldsymbol{R},t)$, less than 10 fs [11–17], due to loss of vibrational wave-function overlap, different rates of phase advance on states 1 and 2, and internal conversion [decay of a_1 and a_2 in Eq. (2), i.e., $a_n\rightarrow a_n(t)$] [11,12]. This has led to a significant debate over the role that electronic coherences play in photosynthesis and other natural processes driven by light absorption [18,19]. Here, we expand upon our recent work [20] and explore electronic coherences in molecules where the potential-energy surfaces of the electronic states in question are approximately parallel and the normally entangled wave function can be roughly factored. This mitigates vibrational dephasing and maintains vibrational overlap for longer times, allowing for $\rho_{12}(\boldsymbol{R},t)$ to survive even in the face of averaging over $\boldsymbol{R}$. Whereas in our previous publication we focused on an experimental demonstration of the coherence and numerical calculations of the relevant potential-energy curves [20], here, we develop some analytical expressions for the measured yield and explore the preparation (via multiphoton excitation) and probing (via ionization) of the wave packet.

II. MEASUREMENT APPROACH

In our experiments, a pump pulse, which can be written as $E_{\rm pu}(t)=E_0(t)\cos(\omega_0 t)$, prepares a wave packet described by Eq. (1) via multiphoton absorption. This is illustrated in Fig. 1, which shows N-photon absorption to state 1 and $(N+1)$-photon absorption to state 2, with $N=4$ for the specific experiments described here. Here, we focus on neutral states of the molecule, in contrast to earlier work that considered ionization to launch an electronic wave packet [2,17,21–23].

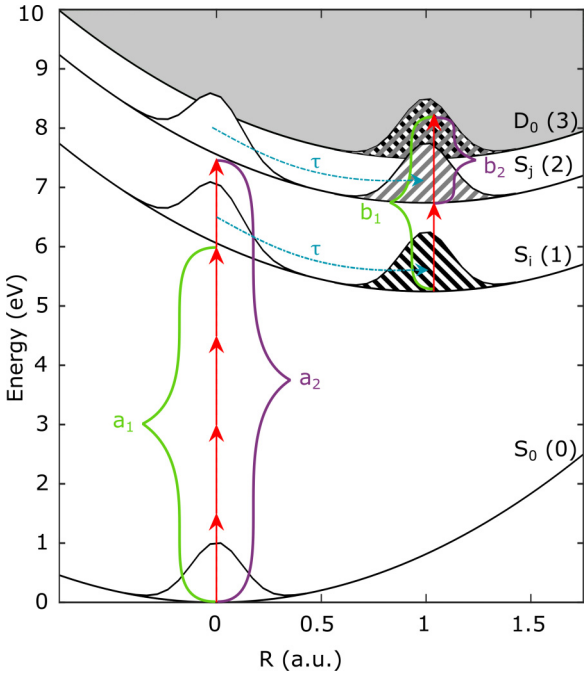

FIG. 1. Cartoon potential-energy curves for a four-state system with ground state S_0; two excited states, S_i and S_j; and ionic state D_0, which are referred to as states 0, 1, 2, and 3, respectively. The red arrows describe the multiphoton coupling photon orders, and the coefficients a and b describe the multiphoton coupling strengths, where a describes the excitation and b describes the ionization.

Impulsive multiphoton ionization with a phase-locked probe pulse at time τ ($E_{\rm pr}(t) = E_0'(t-\tau)\cos[\omega_0(t-\tau)-\phi]$) produces an ionization yield that can be written as

$$Y(t,\tau,\phi) = |a_1|^2|b_1|^2 + |a_2|^2|b_2|^2 + b_1 b_2^* \int d\boldsymbol{R}\rho_{12}(\boldsymbol{R},t) + \text{c.c.}, \tag{3}$$

where we neglect nonadiabatic coupling between the states, thus taking a_1 and a_2 to be time independent, as noted in the previous section. Here, b_1 and b_2 represent m and $m-1$ photon ionization amplitudes (with $m=2$ in this work), which are proportional to the mth and $(m-1)$th powers of the probe-pulse field, respectively:

$$b_1(t) = Q_{1\rm f}(E_{\rm pr}(t))^m, \tag{4a}$$

$$b_2(t) = Q_{2\rm f}(E_{\rm pr}(t))^{(m-1)}. \tag{4b}$$

Here, $Q_{1\rm f}$ and $Q_{2\rm f}$ represent field-independent multiphoton matrix elements that can be written in terms of sums over off-resonant intermediate states [24,25]. If one writes a delay-dependent phase on the probe pulse given by $\phi = \phi_L - \omega_L\tau$, where ω_L is a locking frequency discussed below, then the yield as a function of the pump-probe delay and phase can finally be written as (see the Appendix for details)

$$Y(\tau,\phi) = |a_1|^2|Q_{1f}(E_0')^m|^2 + |a_2|^2|Q_{2f}(E_0')^{(m-1)}|^2 + a_1 a_2^* Q_{1\rm f}Q_{2\rm f}^*(E_0')^{(2m-1)} \int d\boldsymbol{R}\chi_1(\boldsymbol{R},\tau)\chi_2^*(\boldsymbol{R},\tau) \times e^{i[(\omega_{21}-\omega_L)\tau+\phi_L]} + \text{c.c.} \tag{5}$$

III. EXPERIMENTAL APPARATUS

Equation (5) highlights the fact that excitation and ionization with a phase-locked pulse pair where ϕ can be controlled allow for measurements of the coherence between states 1 and 2, provided that integration over $\boldsymbol{R}$ does not wash it out. The generation of such a controllable phase-locked pulse pair can be achieved through the use of an optical pulse shaper.

Our experiments make use of an amplified Ti:sapphire laser system which produces transform limited 30-fs laser pulses with an energy of 1 mJ at a repetition rate of 1 kHz. The pulses are spectrally broadened in a 2.1-m-long 450-μm-core stretched hollow-core fiber filled with 600 Torr of ultrahigh-purity argon gas. The input spectrum centered around 780 nm is blueshifted to 750 nm and broadened from 600 to 900 nm [26–28].

An acousto-optic-modulator- (AOM) based pulse shaper [29] is used for compression, characterization, and shaping of these ultrabroadband pulses. In the pulse shaper the AOM is used as a spectral mask $M(\omega)$ to shape the pulse in the frequency domain by placing it in the Fourier plane of a zero-dispersion stretcher [30]. The shaped electric field $E'(\omega)$ is a product of the acoustic mask $M(\omega)$ and the unshaped field $E(\omega)$: $E'(\omega) = M(\omega)E(\omega)$. Using a phase mask modeled by a Taylor-series expansion up to fourth-order dispersion combined with the residual reconstructed phase from a pulse-shaper-assisted dispersion scan [28], the broadened spectrum is compressed to the near transform limit, 7 fs. The pulse can be further characterized temporally using a pulse-shaper-assisted, second-harmonic-generation collinear frequency-resolved optical gating technique [31,32] which confirms the 7-fs pulses.

For the experiments we explore multiple mask functions. One is modeled by a Gaussian to narrow the optical spectrum and perform measurements with different central optical frequencies. This equation is written as

$$M(\omega) = A\exp\left(-\frac{(\omega-\omega_c)^2}{\Delta_\omega^2}\right) = M_{\rm WS} \tag{6}$$

where A is the overall amplitude, ω_c is the optical frequency at which the chosen window is centered, and Δ_ω is the width of the narrowed optical bandwidth. Another mask function generates a pulse pair with independent control over both the pump-probe delay τ and the relative phase between the pulses ϕ_L while establishing a locking frequency ω_L and is written as

$$M(\omega) = A_T(1 + A_R e^{i(\omega-\omega_L)\tau + i\phi_L}) = M_{\rm PP}, \tag{7}$$

where A_T is the overall amplitude and A_R is the relative pump-probe amplitude such that $E_0'(t) = A_R E_0(t)$. A_T is adjusted to maintain a similar intensity when changing the pulse duration, and A_R is set to 0.7 for a 2:1 intensity ratio between the two pulses [20]. The relative phase between pulses described by the probe pulse ϕ can be expressed in terms of ϕ_L and ω_L by $\phi = \phi_L - \omega_L\tau$. This leads to the two different phase-sensitive measurements that we carried out, which were to directly scan ϕ_L for a fixed value of τ (phase measurement), and to vary τ (pump-probe measurement).

Finally, we note that combining the two mask functions, $M(\omega) = M_{\rm WS}M_{\rm PP} = M_{\rm WPP}$, allows us to perform a

pump-probe measurement for narrowed spectra at different central frequencies.

These shaped pulses are then focused in an effusive molecular beam inside a vacuum chamber with a base pressure of $\sim 10^{-10}$ Torr, raising the working pressure to about $\sim 10^{-6}$ Torr. The molecules are ionized by the laser pulses, with peak intensities of up to $\sim 10^{13}\,\mathrm{W/cm^2}$. The electrons generated by ionization are velocity map imaged to a dual-stack microchannel plate and phosphor screen detector using an electrostatic lens. The light emitted by the phosphor screen at each position is recorded by a complementary metal-oxide semiconductor camera. The camera measurements are inverse Abel transformed to reconstruct the three-dimensional momentum distribution of the outgoing electrons and the photoelectron spectrum (PES). The following measurements describe the photoelectron spectrum or yield as a function of the various pulse-shaper parameters.

IV. ELECTRONIC STRUCTURE CALCULATIONS

In order to aid in the interpretation of the experimental results we performed electronic structure calculations. The equilibrium geometry of the ground electronic state and singlet excited-state energies of thiophene at this geometry were determined by the electronic structure calculations described in Ref. [25]. The geometry optimization was performed by density-functional theory using the GAUSSIAN program package [33] with the Becke three-parameter Lee-Yang-Parr (B3LYP) functional [34,35] and augmented correlation-consistent polarized valence triple zeta (aug-cc-pVTZ) basis set [36] for all the atoms. The state energies were determined at the multistate complete-active-space second-order perturbation theory level [37] for 30 states with the help of the OPEN-MOLCAS 20.10 program package [38]. The active space consisted of 10 electrons and 11 orbitals. (The shapes of the active orbitals are displayed in Fig. 10 of Ref. [25].) For further details of the computations see Ref. [25].

V. MEASUREMENTS

As described in the Introduction and Sec. II, the electronic coherences are driven by multiphoton absorption and probed via ionization. This excitation and ionization process can be described in terms of resonantly enhanced multiphoton ionization (REMPI), in which two resonances are driven simultaneously and interfere in the ionization yield.

A. Multiphoton resonance

We first demonstrate REMPI by working with the pulse-shape parametrization described above, which produces a narrowband pulse whose central frequency can be scanned across the full laser spectrum. Figure 2 describes the experiment utilizing the M_{WS} mask [Eq. (6)]. Here, Δ_ω was fixed at 0.078 rad/fs, which corresponds to a 35-fs pulse. The central optical frequency ω_c was scanned across the optical spectrum, and the PES at each frequency was measured. The top panel of Fig. 2 shows the PES as a function of photon energy (optical frequency), with each individual PES normalized to the total ionization yield (integral of the PES). This allows for clearly seeing the spectrum as a function of photon

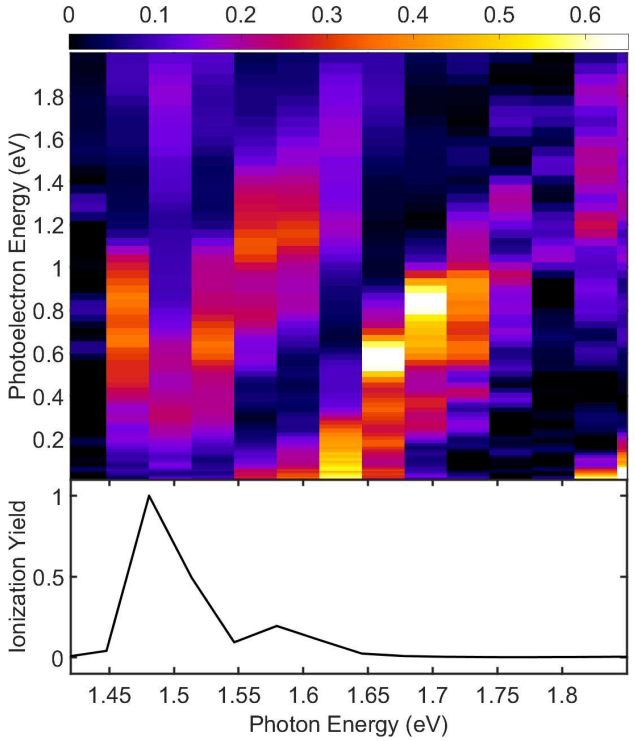

FIG. 2. Normalized photoelectron yield as a function of photoelectron kinetic energy and photon energy (top panel) and total ionization yield (integral of the un-normalized PES) vs photon energy (bottom panel). The top panel shows the PES as a function of photon energy after dividing by the total ionization yield at each photon energy.

energy but does not allow for comparing the yields at different photon energies. To account for this, the bottom panel plots the total ionization yield as a function of photon energy normalized to the maximum, allowing for a comparison of the yields at different photon energies. The yield clearly varies dramatically, with a peak near a photon energy of 1.5 eV as a result of resonant enhancement of the multiphoton ionization. This resonant enhancement also leads to an interruption in the diagonal line pattern of the top panel (near 1.50 eV there is a noticeable smearing or doubling of the photoelectron peak) since near the resonant enhancement the photoelectron peak (energy K) does not shift smoothly with photon energy, as one expects for the photoelectron energy associated with nonresonant ionization:

$$K = n\hbar\omega_0 - I_p - U_p, \tag{8}$$

where $\hbar\omega_0$ represents the photon energy, n represents the multiphoton order, I_p is the ionization potential (8.9 eV for thiophene), and U_p is the ponderomotive potential ($<$0.5 eV).

These measurements highlight the first, albeit trivial, condition for measuring coherence—there needs to be a strong multiphoton resonance coupling the ground state to the excited states of interest.

B. Interference

Having established the importance of multiphoton resonances in enhancing the ionization yield, we now turn to

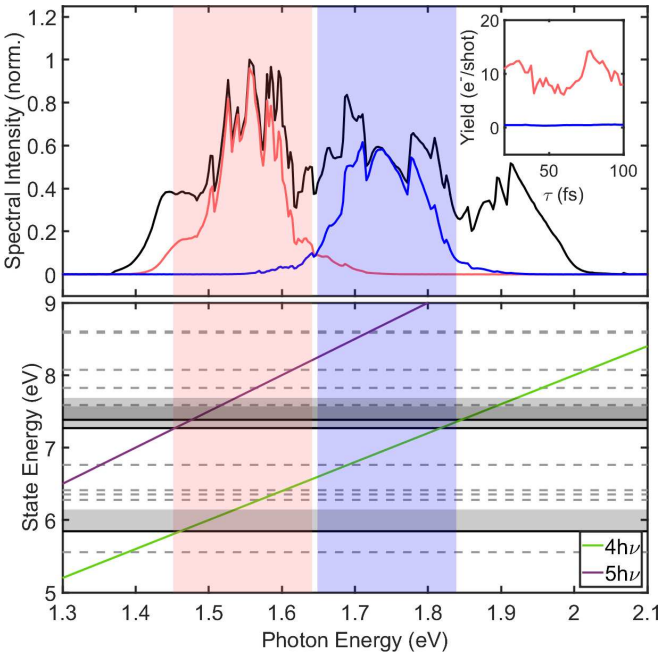

FIG. 3. Top: optical spectra, with the full spectrum in black and two narrowed spectra in red and blue, centered at 1.55 and 1.74 eV, respectively. Inset: pump-probe measurements using the two narrowed spectra color-coded accordingly. Bottom: electronic structure-calculated state energies at the FC geometry (horizontal lines) compared with the four- (green) and five- (purple) photon excitation energies (diagonal lines). States for which the potential-energy surfaces are parallel are shown with black lines, whereas all of the other states are shown with dashed gray lines. The grey shading illustrates the range of Stark shifted energies for the states with parallel potentials.

measurements with the combined mask M_{WPP} to perform a pump-probe measurement for narrowed spectra at different optical frequencies to establish the possibility of interference between two or more resonance enhancements. Here, Δ_ω is set to 0.18 rad/fs, which corresponds to 15-fs pulses. The pump-probe measurement was performed for two central optical frequencies, 2.35 rad/fs (1.55 eV) and 2.65 rad/fs (1.74 eV). The top panel of Fig. 3 shows the optical spectrum as a function photon energy with the full spectrum in black, the spectrum centered at 1.55 eV in red, and that centered at 1.74 eV in blue. The resulting photoelectron yield as a function of pump-probe delay is presented in the inset. We see that the red centered spectrum results in a modulated yield, while the blue centered spectrum is flat and nearly zero. This suggests that within the red spectrum are multiple resonant states which interfere with one another, causing the modulation in the yield. We note that while, in principle, the modulations could come from a vibrational coherence rather than an electronic one, further measurements described below for different locking frequencies make a clear case for electronic coherence.

The bottom panel of Fig. 3 supports this idea by showing the excited-state energies of thiophene at the Franck-Condon (FC) geometry between 5 and 9 eV determined by electronic structure calculations. The state energies are independent of the applied photon energy, so they correspond to flat lines, which are shown purely for clarity so that the state energy can be compared with the excitation energy for four- (green) and five- (purple) photon processes. States for which the potential-energy surfaces are parallel (as seen from earlier electronic structure calculations [20]) are shown in black, whereas all of the other states are shown as dashed gray lines. The range of possible Stark-shifted energies is illustrated by the gray shading for the states with parallel potentials. The key point is that at no point within the blue spectral bandwidth (shaded in blue) do the four- and five-photon lines cross (come into resonance with) a state at the same photon energy. However, there are multiple photon energies (1.45, 1.55, and 1.60 eV, for example) within the red spectral bandwidth (shaded in red) where both four- and five-photon resonances are possible for the same photon energy. This demonstrates both that there can be simultaneous (n)th- and $(n+1)$th-order resonances within the laser bandwidth and that, if there are, they can lead to interference in the ionization yield.

VI. COHERENCE

In order to explore the coherences in more detail and confirm that they correspond to coherences between electronic states, we make use of the entire optical spectrum to perform a pump-probe measurement with the mask M_{PP} [Eq. (7)]. Rather than in a traditional pump-probe experiment where the delay τ is varied without independent control over the relative phase between pulses, we perform a delay-locked phase scan where the delay is fixed and the relative pump-probe phase is scanned from 0 to 4π. This measurement can be repeated for different delays to create the contour plot shown in Fig. 4.

Figure 4 shows the ionization yield as a function of pump-probe delay and phase. These measurements clearly show how the yield varies with phase for all of the measured delays. This phase dependence, which can be described by Eq. (5), indicates that the molecular coherence in question is electronic. Given the one-photon difference between the electronic states, the yield exhibits one modulation per 2π [the ϕ_L term in the exponential part of Eq. (5)]. This modulation has a phase offset given by the first term in the exponential because the phase scan is performed at a fixed delay and a locking frequency that is not equal to the difference in energy between the electronic states. This is highlighted by the lineouts in the top right panel, where we expect a 0.8π phase difference between the phase scans at these delays given the 2.51 rad/fs locking frequency and estimated 2.28 rad/fs (1.5 eV) energy difference (discussed below).

While there is a clear phase dependence to the yield, one can see that the depth of modulation of the yield (D_M = max(signal) − min(signal)/[max(signal) + min(signal)]) also varies with delay (see the bottom panel in Fig. 4). This was previously observed numerically in Ref. [39] and highlights the variation of the vibrational overlap, which modulates the coherence, as described by Eq. (2). Given differences in the shapes of the potentials for the two different excited states, the vibrational wave functions on the two states, $\chi_1(\boldsymbol{R}, t)$ and $\chi_2(\boldsymbol{R}, t)$, will evolve differently and not overlap perfectly (i.e., they will spread, be localized at different $\boldsymbol{R}$, and have different $\boldsymbol{R}$-dependent phases), and this variation in overlap with time

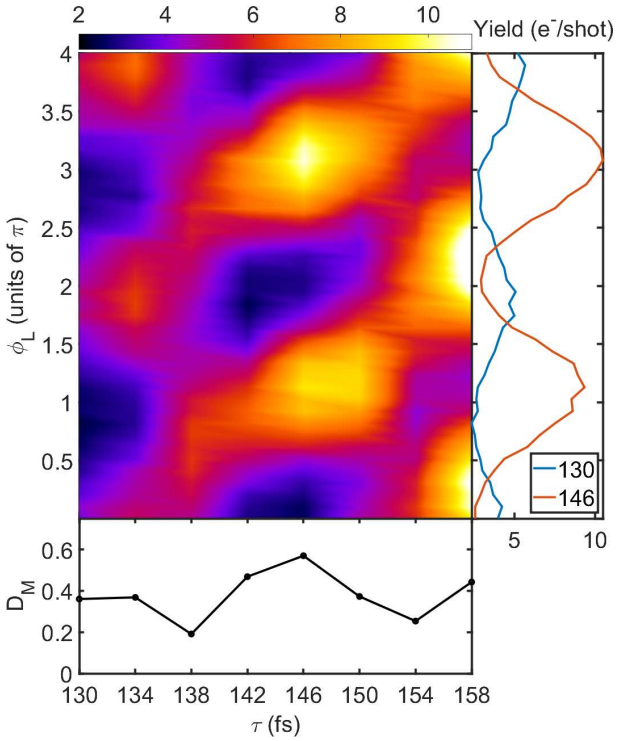

FIG. 4. Top: Measurements of the ionization yield of thiophene as a function of phase for different pump-probe delays. The right panel shows the total yield as a function of phase for two different delays: 130 and 146 fs. Bottom: The depth of modulation D_M in the phase scan as a function of delay, where D_M is evaluated between 0 and 1. The measurements highlight the phase dependence and the variation in depth of modulation with delay, illustrating the influence of the vibrational wave-packet overlap on the measured coherence.

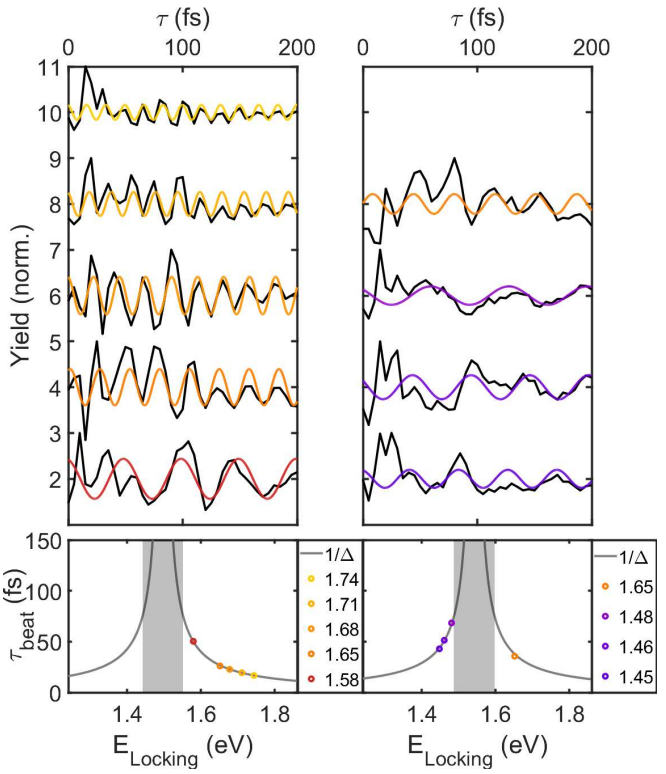

FIG. 5. Pump-probe measurements for different locking frequencies. Top panels show experimental data (black lines) overlaid with sinusoidal fits of the data (colored lines). Top left: electron yields as a function of delay for locking frequencies: 2.40 rad/fs (1.58 eV), 2.51 rad/fs (1.65 eV), 2.55 rad/fs (1.68 eV), 2.60 rad/fs (1.71 eV), and 2.65 rad/fs (1.74 eV). Bottom left: modulation period vs locking frequency for the measurements above. The solid line corresponds to Eq. (9) for a molecular resonance at 1.50 eV. Top right: electron yields as a function of delay for locking frequencies: 2.20 rad/fs (1.45 eV), 2.22 rad/fs (1.46 eV), 2.25 rad/fs (1.48 eV), and 2.51 rad/fs (1.65 eV), measured on a different day with a slightly different peak intensity and laser spectrum. Bottom right: modulation period vs locking frequency for the measurements above. The solid line corresponds to Eq. (9) for a molecular resonance at 1.55 eV.

modulates the electronic coherence. The variation in D_M with τ can be seen as a measurement of the time-dependent vibrational overlap as described by the integral term of Eq. (5).

While Fig. 4 shows the yield as a function of phase and delay for a fixed locking frequency of 2.51 rad/fs, pump-probe measurements for different locking frequencies can help identify the energy difference between the electronic states leading to the modulations, as illustrated in Fig. 5.

Figure 5 shows pump-probe measurements at different locking frequencies [20]. The left and right panels show the results of pump-probe measurements conducted on different days with slightly different excitation conditions (similar but slightly different laser spectra and intensities) for several different locking frequencies (top panels). The variation in modulation period τ_{beat} with locking frequency highlights the electronic coherence and is predicted by Eq. (5):

$$\tau_{\text{beat}} = \frac{2\pi}{(\omega_2 - \omega_1) - \omega_L} \tag{9}$$

for the case of potentials which are roughly parallel (see the Supplemental Material in Ref. [20] for calculations of the relevant potentials). The bottom panels in Fig. 5 show the measured modulation periods together with calculated curves for the case of resonances at 1.50 and 1.55 eV. The fact that the modulation periods in the yield for a given laser intensity and spectrum all lie along the curves in the bottom two panels indicates that coherences between pairs of states can dominate the interference in the ionization yield. However, the energy separation between the pair of states changes between measurements, indicating that the interference is more complicated and can involve more than two states [40]. This is not surprising, given the density of states at the four- and five-photon excitation levels and the broad bandwidth of our laser pulses. So while only one pair of states needs to be resonant at the same photon energy to give rise to this coherence, it is possible to have multiple pairs of states resulting in the beating between coherences. For example, the measured resonance of 1.55 eV in Fig. 5 is consistent with the expected resonances in the lower half of Fig. 3. The resonance of 1.50 eV is not as readily obvious. While it could be true that this pair of states is the main one excited due to the particular laser-molecular conditions, an alternative explanation is that the 1.50-eV coherence comes from equal excitation of the 1.55- and the 1.45-eV pairs and arises as the beating of these pairs of states.

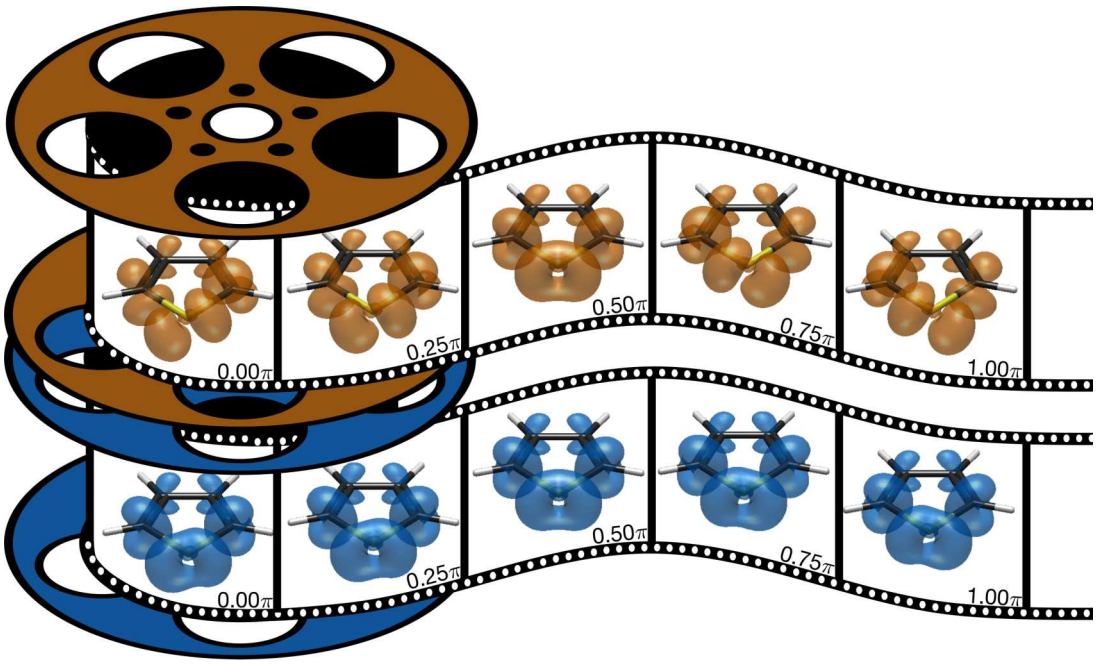

FIG. 6. Selected frames (for different values of $\omega_{21}t$) of two molecular movies showing the evolution of the electron density of a coherent superposition of two electronic states overlaid on the molecular structure of thiophene. The plots show the isosurfaces of constant density. The movie frames in orange (top) show the movie with no loss of coherence, while the movie frames in blue (bottom) show the movie when decoherence mechanisms (dephasing or vibrational overlap) damp the coherence.

VII. ELECTRONIC DYNAMICS

Making use of these measurements and calculations, we present a simplified description of the electronic dynamics. Starting from Eq. (1), we consider a superposition of two electronic states, $\psi_1(\boldsymbol{r};\boldsymbol{R})$ and $\psi_2(\boldsymbol{r};\boldsymbol{R})$, and from there describe the electron density $|\tilde{\Psi}(\boldsymbol{r},t)|^2$ as a function of time. We start by taking the integral of the full probability density $|\Psi(\boldsymbol{r},\boldsymbol{R},t)|^2$ with respect to the nuclear coordinate. Then we can rewrite the probability density in terms of the density-matrix elements using Eq. (2) and $\rho_{nn}(\boldsymbol{R},t) = |a_n|^2|\chi_n(\boldsymbol{R},t)|^2$, where $n = 1, 2$. This results in

$$\begin{aligned}|\tilde{\Psi}(\boldsymbol{r},t)|^2 &= \int |\Psi(\boldsymbol{r},\boldsymbol{R},t)|^2 d\boldsymbol{R} \\ &= \int d\boldsymbol{R}\big[\rho_{11}(\boldsymbol{R},t)|\psi_1(\boldsymbol{r};\boldsymbol{R})|^2 \\ &\quad + \rho_{22}(\boldsymbol{R},t)|\psi_2(\boldsymbol{r};\boldsymbol{R})|^2 \\ &\quad + \rho_{12}(\boldsymbol{R},t)\psi_1(\boldsymbol{r};\boldsymbol{R})\psi_2(\boldsymbol{r};\boldsymbol{R})^* + \text{c.c.}\big]. \end{aligned} \tag{10}$$

If we approximate the integral in Eq. (10) to vary slowly on the timescale of an electronic oscillation period, then the electronic wave functions ψ_n can be treated as nuclear coordinate independent and pulled out of the integral. The a_n coefficients are also $\boldsymbol{R}$ independent. In the first two terms only $\rho_{11}(\boldsymbol{R},t)$ and $\rho_{22}(\boldsymbol{R},t)$ are left within the integral, and for normalized vibrational wave functions, these integrate to 1. What is left of the first two terms is a time- and nuclear-coordinate-independent part of the probability density. Plugging Eq. (2) into Eq. (10) then results in

$$\begin{aligned}|\Psi(\boldsymbol{r},t)|^2 &= |a_1|^2|\psi_1(\boldsymbol{r})|^2 + |a_2|^2|\psi_2(\boldsymbol{r})|^2 + a_1a_2^*\psi_1(\boldsymbol{r})\psi_2(\boldsymbol{r})^* \\ &\quad \int d\boldsymbol{R}(\chi_1(\boldsymbol{R},t)\chi_2^*(\boldsymbol{R},t))e^{i\omega_{21}t} + \text{c.c.} \end{aligned} \tag{11}$$

Using this same timescale approximation, the latter two terms can be simplified as the product of a time-dependent oscillation and an $\boldsymbol{R}$-dependent amplitude. This $\boldsymbol{R}$-dependent amplitude can evolve slowly over an electronic oscillation period but modulates the electronic coherence signal on the timescale of the nuclear dynamics.

Calculations following Eq. (11) on the electronic timescale lead to the molecular movies presented as movie frames in Fig. 6. The movies show how $|\Psi(\boldsymbol{r},t)|^2$ evolves for the case of large vibrational wave-function overlap and low vibrational wave-function overlap. Figure 3 indicates which electronic states are most likely involved in our measurements. Based on this, we used the dominant single-orbital configurations for the two states as the basis for the a_n values, where for a single electronic state the probability density is equal to the square magnitude of the orbital or orbitals involved. The probability density was calculated using these orbitals for values of the $\boldsymbol{R}$-dependent amplitude [integral in Eq. (11)] of 1 for full coherence and 0.25 for low coherence. The frames of the movie are written in terms of $\omega_{21}t$ for half a period of the electronic oscillation (the second half of the oscillation is equivalent to the first half in reverse). In the full-coherence movie in orange (top) we see clear oscillations of the electronic density, particularly surrounding the sulfur atom (yellow) at the front. These density lobes start with a positive slope at a near 45° angle at 0π, shift to no slope by 0.5π, and then continue to a

negative slope at a near 45° angle at 1π. In contrast the movie in blue (bottom) shows much weaker oscillations surrounding the sulfur atom. The oscillations can be described in a similar manner: positive slope at 0π, no slope at 0.5π, and negative slope at 1π; however, the angle of either slope is a few degrees at best, highlighting the damped amplitude of these oscillations. One can note that there is no noticeable change in the electronic density around the carbon atoms opposite the sulfur atom in either movie. This is simply due to the fact that only one of the electronic states leads to nonzero probability for finding the electron around that part of the molecule, resulting in no coherent superposition.

As Fig. 6 illustrates, the coherent superposition of two electronic states shows a variation in the electron density with relative phase, which depends on both $\omega_{12}\tau$ and ϕ_L. Comparing the top and bottom panels, it is clear that the changes in density with phase are more significant in the top panels than in the bottom panels, illustrating how a lower coherence leads to smaller changes in the electron density with time. As the phase between electronic states depends on $\boldsymbol{R}$, integrating over $\boldsymbol{R}$ leads to an averaging over phases between electronic states, which results in less variation in density as a function of the phase difference between states. This is a direct consequence of the entanglement between the electrons and the nuclei. For electronic states with roughly parallel potentials the integration over $\boldsymbol{R}$ does not average over many different phases, and therefore, the coherence and the modulations in electron density with time are more pronounced.

VIII. CONCLUSION

In conclusion, we carried out and analyzed phase-locked pump-probe measurements of electronic wave packets in thiophene, which revealed long-lived electronic coherences between excited states of the molecule. The measurements relied on simultaneous multiphoton resonances at different multiphoton orders (our analysis suggests that there are multiple pairs of electronic states contributing to the measurements), which were facilitated by using ultrabroadband laser pulses. We derived expressions for the ionization yield which can be compared with our measurements. The calculations and measurements illustrate how the coherences evolve with delay between the pump and probe pulses, highlighting the role of vibrations in modulating the coherence. If one is able to measure the nuclei in coincidence with the photoelectrons (e.g., after double ionization with the probe pulse to produce the molecular dication, which can dissociate and produce pairs of fragment ions), then it is also possible to further disentangle the electronic and nuclear dynamics and acquire more insight into their coupled motion [41].

The data that support the findings of this study are not publicly available at this time but may be obtained from the authors upon reasonable request.

ACKNOWLEDGMENTS

This work was supported by the National Science Foundation under Award No. 2110376. T.R. acknowledges support from the National Research, Development and Innovation Fund of Hungary under Grants No. TKP2021-NVA-04 and No. SNN 135636.

The authors declare that they have no conflicts of interest.

APPENDIX

Here, we provide some more details on the derivation of the expressions for the ionization yield as a function of pulse shape provided in the main text. The laser field in time $E(t)$ can be defined as the product of an envelope $E_0(t)$ and a carrier with a frequency of ω_0:

$$E(t) = E_0(t)e^{-i\omega_0 t} + \text{c.c.} \tag{A1}$$

To generate a double pulse with the pulse shaper we apply a mask function $M(\omega)$ to the optical spectrum of the form

$$M(\omega) = 1 + A_R e^{i(\omega-\omega_L)\tau + i\phi_L}. \tag{A2}$$

This mask generates a pulse pair with controllable parameters: relative pulse amplitude A_R, locking frequency ω_L, pump-probe delay τ, and relative pump-probe phase ϕ_L. The locking frequency sets the frequency at which there is always constructive interference in the optical spectrum.

Mathematically, the pulse shaper can be described by Fourier transforming the pulse $E(t) \to E(\omega)$, applying the mask $E'(\omega) = M(\omega)E(\omega)$, and Fourier transforming back $E'(\omega) \to E'(t)$. Here, $E'(t)$ describes the desired shaped laser pulse in the time domain:

$$\begin{aligned} E'(t) &= \int_{-\infty}^{\infty} E'(\omega)e^{-i\omega t}d\omega \\ &= \int_{-\infty}^{\infty} dt E(\omega)e^{-i\omega t} + A_R e^{i(\phi_L-\omega_L\tau)}\int_{-\infty}^{\infty} dt E(\omega)e^{-i\omega(t-\tau)} \\ &= E(t) + A_R E(t-\tau)e^{i(\phi_L-\omega_L\tau)}. \end{aligned} \tag{A3}$$

Using Eq. (A1), we can define the pump and probe pulses by rewriting Eq. (A3). We define the pump pulse as $E_{\text{pu}}(t) = E_0(t)\cos(\omega_0 t)$ and the probe pulse as $E_{\text{pr}}(t) = E_0'(t-\tau)\cos[\omega_0(t-\tau)-\phi]$, where we set $E_0'(t) = A_R E_0(t)$ and simplify the notation for the controllable parameters of the laser as $\phi = \phi_L - \omega_L\tau$.

We can now turn our attention to the experiment and how the laser interacts with the molecule. The pump pulse creates a coherent superposition of electronic states via multiphoton absorption. Reproduced from the main text, Eq. (2) describes the electronic coherence generated by the pump pulse in terms of the off-diagonal elements of the density matrix:

$$\rho_{12}(\boldsymbol{R},t) = a_1\chi_1(\boldsymbol{R},t)a_2^*\chi_2^*(\boldsymbol{R},t)e^{i\omega_{21}t}, \tag{A4}$$

where $\omega_{21} = \omega_2 - \omega_1$.

The ionization step can then be described by

$$Y(t) = |a_1|^2|b_1|^2 + |a_2|^2|b_2|^2 + b_1 b_2^* \int d\boldsymbol{R}\rho_{12}(\boldsymbol{R},t) + \text{c.c.}, \tag{A5}$$

where b_1 and b_2 represent m- and $(m-1)$-photon (with $m = 2$ in this work) ionization amplitudes, which are proportional to the mth and $(m-1)$th powers of the probe-pulse field,

respectively:

$$b_1 = Q_{1f}(E_0'(t-\tau)e^{-i(\omega_0(t-\tau)-\phi)} + \text{c.c.})^m, \quad \text{(A6a)}$$

$$b_2 = Q_{2f}(E_0'(t-\tau)e^{-i(\omega_0(t-\tau)-\phi)} + \text{c.c.})^{(m-1)}. \quad \text{(A6b)}$$

Here, Q_{1f} and Q_{2f} represent field-independent multiphoton matrix elements that can be written in terms of sums over off-resonant intermediate states [24,25].

We consider contributions to the ionization yield that involve the minimum photon orders from states 1 and 2 to arrive at the same final-state energy and make the multiphoton rotating-wave approximation.

Thus, plugging Eqs. (A4) and (A6) into Eq. (A5) and keeping only the relevant terms yield

$$\begin{aligned} Y(t,\tau,\phi) = {} & |a_1|^2|Q_{1f}(E_0')^m(t-\tau)|^2 \\ & + |a_2|^2|Q_{1f}(E_0')^{(m-1)}(t-\tau)|^2 \\ & + a_1a_2^*Q_{2f}(E_0'(t-\tau))^m e^{-im[\omega_0(t-\tau)-\phi]} \\ & \times Q_{2f}^*(E_0'(t-\tau))^{(m-1)}e^{i(m-1)[\omega_0(t-\tau)-\phi]} \\ & \times \int d\boldsymbol{R}\chi_1(\boldsymbol{R},t)\chi_2^*(\boldsymbol{R},t)e^{i\omega_{21}t} + \text{c.c.}, \end{aligned} \quad \text{(A7)}$$

where the final term can be simplified to

$$\begin{aligned} D(t,\tau,\phi) = {} & a_1a_2^*Q_{1f}Q_{2f}^*(E_0'(t-\tau))^{(2m-1)}e^{-i[\omega_0(t-\tau)-\phi]} \\ & \times \int d\boldsymbol{R}\chi_1(\boldsymbol{R},t)\chi_2^*(\boldsymbol{R},t)e^{i\omega_{21}t} + \text{c.c.} \end{aligned} \quad \text{(A8)}$$

The experiment measures the time-integrated yield, $Y(\tau) = \int_{t_1}^{t_2} Y(t)dt$, where t_1 is the time after the pump pulse has been turned off and t_2 is the time after the probe pulse has been turned off. Our interest is in the electronic coherence, so we can focus on this third term, Eq. (A8), which carries all of the phase information. Performing the integral over time results in

$$\begin{aligned} D(\tau,\phi) = {} & a_1a_2^*Q_{1f}Q_{2f}^*e^{i(\omega_0\tau+\phi)}\int_{t_1}^{t_2} dt(E_0'(t-\tau))^{(2m-1)} \\ & \times \int d\boldsymbol{R}\chi_1(\boldsymbol{R},t)\chi_2^*(\boldsymbol{R},t)e^{i(\omega_{21}-\omega_0)t} + \text{c.c.} \end{aligned} \quad \text{(A9)}$$

Upon rearranging the previous equation to account for the integral over time, we make note of two phase terms that arise: $\omega_0\tau + \phi$ and $(\omega_{21} - \omega_0)t$. The first of these is time independent and arises from the probe pulse. It describes the phase advance of the laser as a function of pump-probe delay plus the controllable phase ϕ. The second phase comes from the initial excitation by the pump pulse and describes the phase advance of the coherence with respect to that of the laser.

The pulse durations of the laser pulses are short with respect to the molecular dynamics, and given that the multiphoton ionization signal is another factor of $\sqrt{2m-1}$ shorter than the laser pulse, we continue the analysis in the impulsive limit where $[E_0'(t-\tau)]^{(2m-1)} = (E_0')^{(2m-1)}\delta(t-\tau)$ [42,43]. Thus, $t \to \tau$, and we can rewrite the total phase as $\omega_0\tau + \phi + \omega_{21}\tau - \omega_0\tau$ or $\omega_{21}\tau + \phi$. This simplifies Eq. (A9) to

$$\begin{aligned} D(\tau,\phi) = {} & a_1a_2^*Q_{1f}Q_{2f}^*(E_0')^{(2m-1)}\int d\boldsymbol{R}\chi_1(\boldsymbol{R},\tau)\chi_2^*(\boldsymbol{R},\tau) \\ & \times e^{i(\omega_{21}\tau+\phi)} + \text{c.c.} \end{aligned} \quad \text{(A10)}$$

Finally, we can write the measured yield as

$$\begin{aligned} Y(\tau,\phi) = {} & |a_1|^2|Q_{1f}(E_0')^m|^2 + |a_2|^2|Q_{2f}(E_0')^{m-1}|^2 \\ & + a_1a_2^*Q_{1f}Q_{2f}^*(E_0')^{(2m-1)}\int d\boldsymbol{R}\chi_1(\boldsymbol{R},\tau)\chi_2^*(\boldsymbol{R},\tau) \\ & \times e^{i((\omega_{21}-\omega_L)\tau+\phi_L)} + \text{c.c.}, \end{aligned} \quad \text{(A11)}$$

which remains sensitive to the three decoherence mechanisms described in Eq. (A4). However, the dephasing term is now modified by the applied laser phase, which we have reintroduced as the two types of controllable laser parameters. This gives rise to the two types of pump-probe measurements that can be performed: (1) a delay scan with fixed phase and (2) a phase scan with fixed delay.

[1] H. J. Wörner *et al.*, Struct. Dyn. **4**, 061508 (2017).

[2] A. S. Folorunso, A. Bruner, F. Mauger, K. A. Hamer, S. Hernandez, R. R. Jones, L. F. DiMauro, M. B. Gaarde, K. J. Schafer, and K. Lopata, Phys. Rev. Lett. **126**, 133002 (2021).

[3] S. Haessler *et al.*, Nat. Phys. **6**, 200 (2010).

[4] T. Okino, Y. Furukawa, Y. Nabekawa, S. Miyabe, A. Amani Eilanlou, E. J. Takahashi, K. Yamanouchi, and K. Midorikawa, Sci. Adv. **1**, e1500356 (2015).

[5] T. C. Weinacht, J. Ahn, and P. H. Bucksbaum, Phys. Rev. Lett. **80**, 5508 (1998).

[6] J. A. Yeazell, M. Mallalieu, and C. R. Stroud, Phys. Rev. Lett. **64**, 2007 (1990).

[7] H. Maeda and T. F. Gallagher, Phys. Rev. Lett. **92**, 133004 (2004).

[8] M. Wollenhaupt *et al.*, Phys. Rev. Lett. **89**, 173001 (2002).

[9] M. Born and K. Huang, *Dynamical Theory of Crystal Lattices* (Oxford University Press, Oxford, New York, 1998).

[10] We note that this expansion is slightly different from the standard Born-Huang expansion, for which the a_n coefficient is included in the vibrational wave function $\chi_n(\boldsymbol{R},t)$. We have separated a_n out here since it allows us to use normalized vibrational wave functions and separate the parts of the wave function that are laser dependent from those that are not.

[11] G. J. Halász, A. Perveaux, B. Lasorne, M. A. Robb, F. Gatti, and Á. Vibók, Phys. Rev. A **88**, 023425 (2013).

[12] C. Arnold, O. Vendrell, and R. Santra, Phys. Rev. A **95**, 033425 (2017).

[13] W. Hu, B. Gu, and I. Franco, J. Chem. Phys. **148**, 134304 (2018).

[14] A. Scheidegger, J. Vaníček, and N. V. Golubev, J. Chem. Phys. **156**, 034104 (2022).

[15] H. Hwang and P. J. Rossky, J. Phys. Chem. B **108**, 6723 (2004).
[16] H. Kamisaka, S. V. Kilina, K. Yamashita, and O. V. Prezhdo, Nano Lett. **6**, 2295 (2006).
[17] M. Vacher, M. J. Bearpark, M. A. Robb, and J. P. Malhado, Phys. Rev. Lett. **118**, 083001 (2017).
[18] H.-G. Duan, V. I. Prokhorenko, R. J. Cogdell, K. Ashraf, A. L. Stevens, M. Thorwart, and R. D. Miller, Proc. Natl. Acad. Sci. USA **114**, 8493 (2017).
[19] M. Maiuri, E. E. Ostroumov, R. G. Saer, R. E. Blankenship, and G. D. Scholes, Nat. Chem. **10**, 177 (2018).
[20] B. Kaufman, P. Marquetand, T. Rozgonyi, and T. Weinacht, Phys. Rev. Lett. **131**, 263202 (2023).
[21] D. Schwickert *et al.*, Sci. Adv. **8**, eabn6848 (2022).
[22] M. Ruberti, S. Patchkovskii, and V. Averbukh, Phys. Chem. Chem. Phys. **24**, 19673 (2022).
[23] A. I. Kuleff, N. V. Kryzhevoi, M. Pernpointner, and L. S. Cederbaum, Phys. Rev. Lett. **117**, 093002 (2016).
[24] W. D. M. Lunden, P. Sándor, T. C. Weinacht, and T. Rozgonyi, Phys. Rev. A **89**, 053403 (2014).
[25] B. Kaufman, P. Marquetand, T. Weinacht, and T. Rozgonyi, Phys. Rev. A **106**, 013111 (2022).
[26] M. Nisoli, S. De Silvestri, and O. Svelto, Appl. Phys. Lett. **68**, 2793 (1996).
[27] F. Hagemann, O. Gause, L. Wöste, and T. Siebert, Opt. Express **21**, 5536 (2013).
[28] A. Catanese, B. Kaufman, C. Cheng, E. Jones, M. G. Cohen, and T. Weinacht, OSA Continuum **4**, 3176 (2021).
[29] M. Dugan, J. Tull, and W. Warren, J. Opt. Soc. Am. B **14**, 2348 (1997).
[30] A. M. Weiner, Rev. Sci. Instrum. **71**, 1929 (2000).
[31] R. Trebino, K. W. DeLong, D. N. Fittinghoff, J. N. Sweetser, M. A. Krumbügel, B. A. Richman, and D. J. Kane, Rev. Sci. Inst. **68**, 3277 (1997).
[32] I. Amat-Roldán, I. G. Cormack, P. Loza-Alvarez, E. J. Gualda, and D. Artigas, Opt. Express **12**, 1169 (2004).
[33] M. J. Frisch *et al.*, *GAUSSIAN 09*, Gaussian Inc., Wallingford, CT, 2009.
[34] A. D. Becke, J. Chem. Phys. **98**, 5648 (1993).
[35] C. Lee, W. Yang, and R. G. Parr, Phys. Rev. B **37**, 785 (1988).
[36] K. A. Peterson, D. Figgen, E. Goll, H. Stoll, and M. Dolg, J. Chem. Phys. **119**, 11113 (2003).
[37] J. Finley, P. Åke Malmqvist, B. O. Roos, and L. Serrano-Andrés, Chem. Phys. Lett. **288**, 299 (1998).
[38] I. Fdez. Galván *et al.*, J. Chem. Theory Comput. **15**, 5925 (2019).
[39] A. Csehi, P. Badankó, G. J. Halasz, Á. Vibók, and B. Lasorne, J. Phys. B **53**, 184005 (2020).
[40] While the subtleties of the experimental conditions that lead to these differences are not well known, these measurements are reproducible under similar conditions.
[41] G. Moğol, B. Kaufman, T. Weinacht, C. Cheng, and I. Ben-Itzhak, Phys. Rev. Res. **6**, L022047 (2024).
[42] While the strict impulsive limit, where the field approaches a δ function, is in tension with the multiphoton rotating-wave approximation, we note that our experiments operate in a regime where the pulse is short compared to the nuclear dynamics in question but long compared to the detuning period of the counterrotating terms in the RWA: $1/(\omega_{21} + n\omega_0)$.
[43] B. Kaufman, T. Rozgonyi, P. Marquetand, and T. Weinacht, Phys. Rev. A **102**, 063117 (2020).